Characterization of Onshore Formations in Nova Scotia for CO_2 Storage

Mahsan Basafa[1], *Lucky* Abiashue[1], *Omid* Mohammadzadeh[1], *Michael G.* Babechuk[2], *Alexandre* Plourde[3], *John* Carey[3], *Paul* Durling[3], *Peter* Giles[3], *Carla* Skinner[3], *Lesley A.* James[1,*]

[1] Department of Process Engineering, Faculty of Engineering and Applied Science, Memorial University of Newfoundland, St. John's, NL A1C 5S7, Canada.

[2] Department of Earth Sciences, Faculty of Science, Memorial University of Newfoundland, St. John's, NL A1B 3X5, Canada

[3] Geological Survey of Canada – Atlantic, Natural Resources Canada, 1 Challenger Drive, Dartmouth NS B2Y 4A2

Abstract. Geological carbon storage is critical to meeting Canada's long-term energy needs and climate goals. In Eastern and Atlantic Canada, we are just starting to assess potential geological CO_2 storage sites. The Maritimes and Fundy Basins are large, under-explored Carboniferous sedimentary basins in Eastern Canada and are potential candidates for carbon storage. Mafic and ultramafic rocks offer additional potential carbon storage targets onshore in the region due to their ability to rapidly mineralize CO_2, reducing leakage risk. Comprehensive CO_2 storage assessment includes, but is not limited to, routine core analysis to evaluate storage capacity (porosity) and transmissibility (permeability). Detailed petrographic and mineralogical analysis is crucial to understand potential reactive transport (i.e., dissolution reactions between formation brine, acidified upon injection of CO_2, and minerals in the target formation). In this study, we assess 20 core plug samples from the Boss Point Formation (sandstone) and North Mountain (basalt) in Nova Scotia for potential CO_2 storage. Samples were trimmed to cylindrical shapes, cleaned, and dried to a constant weight difference of ≤ 0.01 g. Porosity was measured using a Helium pycnometer via gas expansion. Permeability was measured using a gas permeameter (steady state method), and then corrected for gas slippage with Klinkenberg correction approach. The mineralogical compositions of these samples were obtained using non-destructive methods of X-ray diffraction (XRD) and X-ray fluorescence (XRF). Porosity and permeability for the Boss Point sandstone were found to range from 10.2 to 18.4% and 0.01 to 3.4 mD, respectively. North Mountain basalt properties were much lower, with 2.7-6.4% porosity and 0.001-0.02 mD permeability. Mineralogical/composition knowledge of rock samples is essential for CO_2 storage site selection and screening. Upon injection, CO_2 dissolves in brine and subsequently carbonic acid forms. The lower pH aqueous phase can react with reservoir rock minerals depending on pressure, temperature, brine salinity and minerals type. Some minerals rapidly dissolve in the acidic brine, potentially leading to localized increases in porosity and permeability, and subsequently change the geomechanical properties. This could weaken the formation especially in the near injection wellbore region. On the other hand, precipitation and potential deposition of some minerals has been observed in the literature which subsequently decreases rock quality and hence damages the CO_2 injectivity. These preliminary assessments are the first step toward screening these two formations for possible future CO_2 storage and helping to determine CO_2 storage capacity and efficiency to assess risks and optimize injection strategies.

Keywords: Geological CO_2 storage, porosity, permeability, mineralogy, geochemistry

[*] Corresponding author: ljames@mun.ca

1 Introduction

The growing need for sustainable energy solutions has motivated the oil and gas sector to investigate geological formations as potential sites for storing CO_2, indicating a promising path towards a more environmentally friendly energy landscape [1-4]. Evaluating these formations is crucial to determine their storage capacity and suitability for injection sites, guaranteeing safe containment, adherence to regulations, and the establishment of efficient monitoring schemes.

The exploration of Eastern and Atlantic Canada manifests the Maritimes and Fundy Basins as promising reservoirs for geological CO_2 storage. As a vast, yet under-explored Carboniferous sedimentary basin, their geological characteristics present a prime opportunity for the implementation of carbon storage initiatives. Moreover, within this region, the presence of mafic and ultramafic rock formations offers additional prospects for CO_2 storage. These rocks possess unique attributes that facilitate rapid mineralization of injected CO_2, thereby mitigating the risk of leakage.

After seismic data and well logs identify the desired formations, core samples are obtained to assess the petrophysical, mechanical, and flow characteristics of reservoir rocks. Petrophysical analysis begins with examining porosity, permeability, and mineral composition [5-7]. Porosity dictates the CO_2 storage capacity of the formation, while permeability influences the movement of CO_2 and the risk of leakage from the reservoir through the sealing caprock. Mineral composition impacts CO_2 trapping, chemical reactions, and the stability of the seal and reservoir. Understanding these properties is essential for evaluating the feasibility, effectiveness, and safety of CO_2 storage projects.

The objective of this study was to assess the petrophysical properties of two potential CO_2 storage reservoirs onshore Nova Scotia, the Boss Point Formation (sandstone) and the North Mountain Basalt, to determine the suitability of these geological units for CO_2 storage. This will facilitate informed decision making on permitting and infrastructure investment related to CO_2 storage.

2 Geological Setting

The Boss Point Formation is a roughly kilometre-thick sandstone-rich sedimentary rock [8]. The Boss Point Formation is widely distributed within the Cumberland sub-basin, part of the complex assemblage of upper Paleozoic structural basins collectively known as the Maritimes Basin (Figure 1). The sub-basin consists of several synclines separated by uplifted and faulted basement blocks [9] in northern Nova Scotia and southeastern New Brunswick. The Boss Point Formation is an Upper Carboniferous unit dominated by fine to medium grained grey sandstones lying at the base of the Cumberland Group [10]. It is characterized by large channel fill complexes up to 120 m thick that can be traced laterally in outcrop for more than 7 km and are interbedded with predominantly grey siltstones that comprise approximately 20% of the succession [11]. The interval is 1125 m thick at its type section [12]; a lithologically similar interval more than 1200 m thick is present in the subsurface at the Gulf Hastings No. 1 well [13]. At its type section, the Boss Point is overlain by the Little River, Joggins and Springhill Mines Formations, which are clastic intervals containing significant amounts of mudstones and coal [10]. In the Hastings well, the overlying 700 m succession is similarly heterolithic, but less coal-rich [13]. These mud-prone rocks could potentially form a seal for potential CO_2 reservoirs in the Boss Point Formation.

The North Mountain Basalt is a widespread unit within the Fundy Basin, an early Mesozoic rift basin beneath the Bay of Fundy and adjacent areas of Nova Scotia and New Brunswick (Figure 1) [14]. The formation comprises numerous basalt flows associated with the development of the Central Atlantic Magmatic Province in the latest Triassic [15]. Where it outcrops along 80 km of the southern shore of the Bay of Fundy (Figure 1), it is typically about 250 m thick [16]. Seismic mapping indicates that it is widely distributed beneath the Bay of Fundy [15]. The middle or Margaretsville Member of the formation has a maximum observed thickness of 170 m and is characteristically vesicular, making it of particular interest for carbon storage [16].

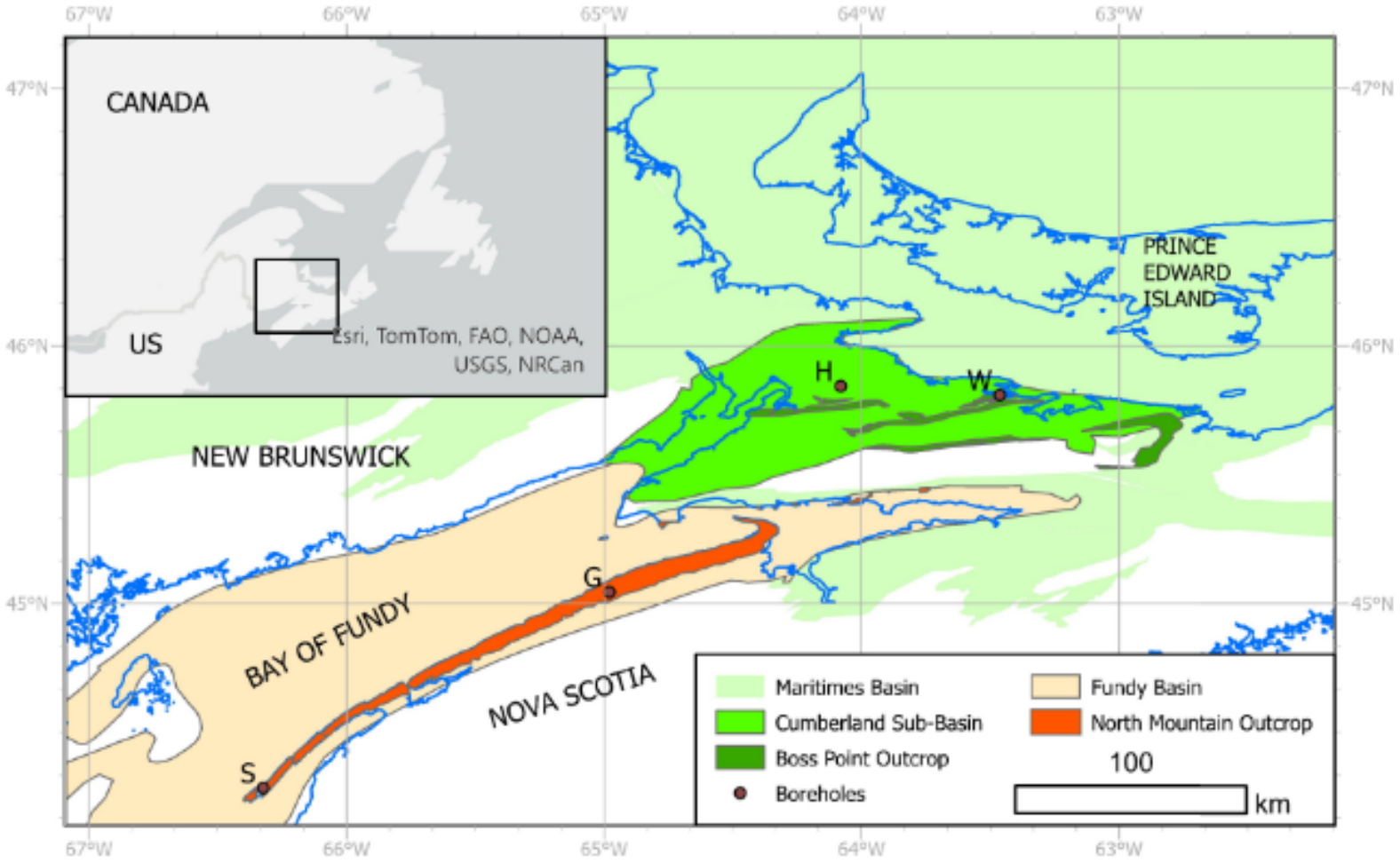

Fig. 1. Location map showing locations and geologic features mentioned in the text. Borehole locations shown are WAL 86-05 (W), Gulf Hastings No. 1 (H), Getty Mines GAV-77-02, and Sladen (S). Also shown is the location of the Boss Point type section (B).

3 Methodology

3.1 Core Plugs Preparation and Cleaning

Ten sandstone samples were collected from the WAL 86-05 borehole (Fig. 1). This area is mapped as Boss Point due to its similar lithological characteristics [17], although palynological work indicates that it may be temporally correlative with the younger formations overlying the Boss Point at its type section [9]. Ten basalt samples were collected from the Getty Mines GAV-77-02, the Sladen boreholes (Fig. 1) that contain the targeted Margetsville Member.

The obtained core plug samples were trimmed to a cylindrical shape. Prior to routine core analysis, the cleaning and drying was performed using chemical solvents to remove oil residuals, water, evaporated salts, mud filtrate, and other contaminants from the core samples [18, 19]. Some preliminary XRD tests were conducted on some randomly selected core plugs from each rock type category. These preliminary XRD analysis revealed the presence of some sensitive clay minerals in a sub-set of core plugs that necessitated the selection of a mild cleaning protocol (i.e., cold solvent flow-through). In this method, isopropanol was injected through each individual core plug at room temperature for several pore volumes until clear solvent outflow was observed. The solvent was then switched to methanol, and the same procedure was followed until clear solvent discharged at the coreflooding exit end. This mild cleaning process preserves sensitive clays such as muscovite and illite. After cleaning, the core plug samples were dried in a convection oven at 40°C, with daily weight measurements until the weight difference was below 0.01 g between three last consecutive measurements, showing end of the drying process.

3.2 Porosity Measurement

A Helium gas expansion porosimeter was used to measure porosity of the cleaned core plug samples. This method enables the determination of sample's pore volume via an isothermal helium expansion and the application of Boyle's law. In this method, a calibration curve is generated by monitoring the equilibrium pressure of helium gas when expanded from the standard chamber (valve 3 to valve 2) to the sample chamber (valve 3 to valve 1) as seen in Fig. 2. To prepare the calibration curve, 11 standard cylindrical steel samples of different known pore volumes were manufactured and tested in the gas pycnometer at an overburden pressure of 400 psig and initial pressure of 26.360 ± 0.01 psig. After generating the calibration curve, the core plug samples were placed in the sample chamber, and the same procedure was carefully followed to determine the equilibrated pressure difference, based on which the pore volume was determined from the calibration curve. The core plug sample bulk volume was calculated by measuring the length and diameter of the sample thrice and taking the average. Porosity was calculated by dividing the pore volume by bulk volume.

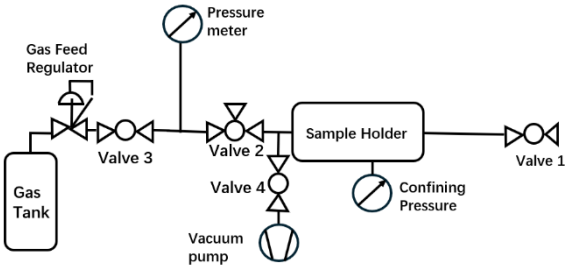

Fig. 2. Schematic diagram of the porosimeter

3.3 Permeability Measurement

Permeability characterizes the ease with which fluids flow through a porous medium in response to an applied fluid pressure gradient. Klinkenberg permeability, which was first established by L. Klinkenberg [20], compensates for gas slippage at the pore wall. Klinkenberg permeability is lower than gas permeability and approximately the same as single-phase liquid permeability.

Permeability to air was measured using a steady-state routine gas permeameter containing a hassler-type core holder. The core plug sample was sealed into a rubber sleeve in the hassler core holder using a confining pressure of 400 psig. Gas (helium) flow was introduced across the sample, and after a constant flow rate was established, the differential pressure across the core sample and gas flow rate was measured. Back pressure was created, and the same process was repeated for at least three increasing pressure steps. The calculated gas permeabilities (K_g) at various flow rates and pressure conditions were plotted against the inverse of mean pressure ($1/P_m$). A linear correlation was fitted to the data points, and the intercept was used to obtain the Klinkenberg corrected permeability. The gas permeability (k) is calculated applying Darcy's law as follow [21]:

$$K_g = \frac{2000 Q_1 P_1 \mu L}{A(P_1^2 - P_2^2)} \quad (1)$$

where P_1 is the inlet pressure (psig), P_2 is the outlet pressure (psig), μ is the viscosity of helium (cP), A is the surface area of the porous medium (cm^2), and Q is the flow rate (cm^2/s).

3.4 Mineralogical and Geochemical Analysis

To supplement the petrophysical data, a set of mineralogical and geochemical analyses were conducted on some selected basalt samples. The tests consist of X-ray diffraction (XRD) crystallography along with quantitative determination of major elements in the rock

samples with X-ray fluorescence (XRF). Fragments obtained from trimming the core plug samples were crushed with a benchtop jaw crusher and then pulverized with a ball mill with agate insert (Retsch PM100) or, for smaller samples, with a hand agate mortar and pestle. The produced powders were split for X-Ray diffraction (XRD) and X-ray fluorescence (XRF) spectrometry analyses in The Earth Resources Research & Analyses (TERRA) node of the Memorial University of Newfoundland (MUN), Core Research & Instrument Training (CREAIT) Network.

In preparation for geochemical analysis, weighed aliquots of sample powder were heated to 1050°C to determine bulk volatile content from the loss on ignition (LOI). The ignited powders were combined with a mixed Li-metraborate/-tetraborate flux into platinum crucibles and fused to prepare a glass disc with a Katanax X-600 electric fusion instrument. All glass discs were measured in the same experiment on a Bruker S8 Tiger sequential wavelength-dispersive XRF. Calibration was accomplished with a suite of geological reference materials covering a range in abundances for all analyte elements. These analyses provide a quantitative determination of major elements in the rock samples.

In preparation for mineralogical analyses, powder sample was pressed into a sample holder and smeared on the surface to randomize grain orientation. The XRD spectra were collected on a Rigaku Ultima IV operated 40 kV/44 mA with a copper x-ray source and a scintillation counter detector. The spectra were collected across a 2θ angle range of 3-90° at 0.02° steps using the instrument's continuous scanning mode. The MDI JADE software, with a comprehensive database for natural geological materials, was used for analyzing X-ray powder diffraction data and mineral identification.

4 Results and Discussion

4.1 Porosity and Permeability Measurements

The results of porosity measurements for the basalt (SG01 – SG19) and sandstone (SW01 – SW19) samples are given in Table 1.

Table 1. Porosity and permeability of the basalt and sandstone samples

Sample ID	Porosity (%) (± 2%)*	Permeability (mD) (± 5.1%)**
Basalt		
SG-01	2.40 ± 0.30	0.0001
SG-03	3.30 ± 0.06	0.0003
SG-05	5.80 ± 0.10	0.16
SG-07	8.50 ± 0.20	0.005
SG-09	3.80 ± 0.50	0.01
SG-11	4.50 ± 0.30	0.003
SG-13	3.20 ± 0.20	0.001
SG-15	10.50 ± 0.40	0.003
SG-17	6.40 ± 0.00	0.003
SG-19	4.10 ± 0.20	0.0007
SLA-03	3.10 ± 0.02	0.005
SLA-05	10.20 ± 0.03	1.89
Sandstone		
SW-01	7.30 ± 0.10	0.034
SW-03	15.40 ± 0.03	3.36
SW-05	4.80 ± 0.40	0.01
SW-07	3.30 ± 0.30	0.45
SW-09	14.40 ± 0.20	1.08
SW-11	13.10 ± 0.10	1.48
SW-13	14.0 ± 0.44	1.64
SW-15	10.60 ± 0.10	2.97
SW-17	14.6 ± 0.02	3.07
SW-19	17.50 ± 0.80	0.38

*Relative measurement uncertainty for porosimetry method
**Relative measurement uncertainty for permeametry method

The porosity of basalt samples was below 10.2%. SG-15 has the highest porosity of 10.1%, while SG-01 has the lowest porosity of 2.4%. Most of the the sandstone samples have porosities above 10.0%. Among the sandstone samples, the highest porosity is 17.5% for SW-19 and the lowest porosity is 3.3% for the sample SW-07.

The basalt samples generally show very low permeabilities, i.e., 0.17 mD. The sandstone samples have higher permeability values compared to the basalt samples with the highest permeability of 3.36 mD for the sample SW-03. The porosity measurements were done three times per sample and the ± values reported in Table 1 (middle column) are the standard deviation associated with the mean for every core plug sample. A sample plot for Klinkenberg permeability determination using linear regression for multiple gas permeability measurements is shown in Fig. 3. The R^2 values associated with linear regressions for these graphical Klinkenberg corrections were all above 0.9000.

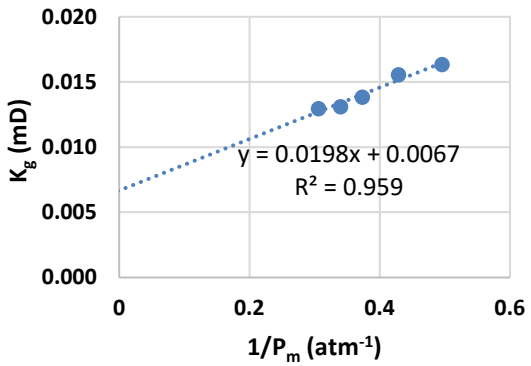

Fig. 3. Klinkenberg permeability plot for sample SG-09

4.2 Mineralogical and Geochemical Studies

The XRF data of the basalt and sandstone samples are given in Tables 2 and 3, respectively. The oxides identified through XRF analysis are SiO_2, TiO_2, Al_2O_3, Fe_2O_3, MgO, MnO, CaO, Na_2O, K_2O, and P_2O_5. The most abundant oxide observed in the samples was SiO_2 with its content varying between 47.02 wt% and 51.62 wt% in the basalt samples and 81.55 wt% and 83.97 wt% in the sandstone samples. Al_2O_3 and Fe_2O_3 were noted as the next most abundant oxides in the basalt samples with their content ranging within the limits of 13.29 – 13.79 wt% and 10.71 – 12.24 wt%, respectively. The Al_2O_3 and Fe_2O_3 content of the sandstone samples were lower compared to the basalt samples, i.e., 6.66 – 8.39 wt% and 2.66 – 3.39 wt%, respectively.

The major element oxide abundances of the basalt samples are as expected for basalt (e.g., plotting in the basalt field of the total alkalis-silica (TAS) diagram or in a range of Ca+Na/Al ratios that do not indicate prominent alteration of groundmass plagioclase to clays; not shown) with some notable minor deviations. More specifically: (1) sample SG-09 has a higher K than other samples and corresponds with a pinker-coloured groundmass of the sample relative to others; (2) the LOI is higher than typical for freshly erupted basalt (<3 wt.%) in samples showing macroscopic evidence for amygdale in-fills (SG-01, -07, and -11) indicating that later-stage amygdale minerals include hydrous low-temperature minerals for which identification is in progress.

Table 2. Chemical composition (major element concentrations expressed as weight percent of oxides) and geochemical weathering parameters (CIA, MIA, ICV) for the basalt samples.

Sample	SG-01	SG-07	SG-09	SG-11
Oxides (wt%)				
SiO_2	51.31	48.66	51.62	47.02
TiO_2	1.199	1.325	1.142	1.351
Al_2O_3	13.29	13.45	13.79	13.32
Fe_2O_3(T)	10.71	11.86	11.18	12.24
MgO	5.37	6.51	6.75	6.50
MnO	0.162	0.178	0.169	0.169
CaO	9.05	9.70	10.08	9.93
Na_2O	2.42	1.84	2.38	2.14
K_2O	0.40	0.91	1.17	0.19
P_2O_5	0.149	0.165	0.138	0.165
LOI	4.78	5.47	1.35	6.72
Total	98.85	100.06	99.77	99.76
CIA	39.1	38.6	37.2	38.2
MIA_O	37.0	35.7	34.1	35.7
ICV	2.21	2.40	2.38	2.44

Table 3. Chemical composition (major element concentrations expressed as weight percent of oxides) and geochemical weathering parameters (CIA, MIA, ICV) for the sandstone samples.

Sample	SW-13	SW-15	SW-17	SW-19
Oxides (wt%)				
SiO_2	83.97	82.35	81.89	81.55
TiO_2	0.813	0.523	0.449	0.527
Al_2O_3	6.66	7.89	7.94	8.39
Fe_2O_3(T)	3.39	2.93	3.12	2.66
MgO	0.65	0.66	0.67	0.53
MnO	0.023	0.025	0.037	0.015
CaO	0.15	0.17	0.28	0.13
Na_2O	1.11	1.45	1.46	1.48
K_2O	1.33	1.57	1.58	1.77
P_2O_5	0.083	0.081	0.059	0.077
LOI	1.23	1.45	1.67	2.11
Total	99.41	99.12	99.17	99.26
CIA	65.9	64.7	63.5	65.1
MIA_O	63.5	62.1	61.3	63.3
ICV	1.12	0.93	0.96	0.85

The mineralogical and chemical compositions of sedimentary rocks provide important information about the source rock composition, the weathering degree, duration of weathering, and mechanisms of transportation and depositional processes [22, 23]. Depending on temperature, precipitation, exposure age, and geomorphological coditions, chemical weathering results in changes of compositions, mineral phases, and textural features compared to the fresher parental rock [24, 25].

During chemical weathering, chemical elements are mobilized and their variations between the fresher rocks and the weathered products are determined by the intensity of chemical weathering processes. In particular, mobile elements such as K, Na, Mg, and Ca tend to be leached out during weathering processes, whereas immobile elements such as Al, Fe, and Ti are stored in stable weathering products and experience minor losses [26, 27]. Following chemical weathering and erosion, sediment will further undergo hydrodynamic sorting during transport prior to deposition.

The depletion of mobile elements relative to immobile elements during weathering processes is measured by geochemical weathering indices such as Chemical Index of Alteration (CIA) and the Mafic Index of Alteration (MIA) [28-31]. These indices can monitor the in-situ chemical weathering of crystalline rocks, but are also influenced by further sedimentary processes upon erosion and transport of weathered materials. The CIA is the most used indicator based on the ratio of immobile Al element to major mobile elements, i.e., K, Na, and Ca, tracking primarily feldspar weathering, and is calculated as follows:

$$\mathrm{CIA} = \mathrm{Al_2O_3}/(\mathrm{Al_2O_3} + \mathrm{K_2O} + \mathrm{Na_2O} + \mathrm{CaO^*}) \times 100 \quad (2)$$

Another chemical weathering index which extends the equation of CIA to include the mafic elements Mg and Fe is the MIA. Depending on the redox conditions of the alteration environment, the MIA is calculated as follows [30]:

$$\mathrm{MIA_O} = \left(\mathrm{Al_2O_3} + \mathrm{Fe_2O_{3(T)}}\right)/\left(\mathrm{Al_2O_3} + \mathrm{Fe_2O_{3(T)}} + \mathrm{MgO} + \mathrm{Na_2O} + \mathrm{CaO^*} + \mathrm{K_2O}\right) \times 100 \quad (3)$$

$$\mathrm{MIA_R} = \mathrm{Al_2O_3}/\left(\mathrm{Al_2O_3} + \mathrm{Fe_2O_{3(T)}} + \mathrm{MgO} + \mathrm{Na_2O} + \mathrm{CaO^*} + \mathrm{K_2O}\right) \times 100 \quad (4)$$

Under oxidative weathering conditions where Fe is retained by the formation of insoluble ferric iron (Fe^{3+}) oxides, total Fe is considered an immobile element along with Al and the MIA is calculated as Eq. 3. However, in reducing environments where ferrous iron (Fe^{2+}) can be mobile and leached along with Mg, Eq. 4 is used to calculate the MIA.

In the above mentioned equations, all variables represent the molar amounts of major-element oxides. The CaO^* is the amount of CaO incorporated into the silicate fraction of rocks without contributions of CaO from carbonate and phosphate minerals, and is calculated as follow [30]:

$$\mathrm{CaO^*} = \text{moles CaO} - \text{moles } \mathrm{CO_{2(calcite)}} - (0.5 \times \text{moles } \mathrm{CO_2})_{\text{dolomite}} - [(10/3) \times \text{moles } \mathrm{P_2O_5}]_{\text{apatite}} \quad (5)$$

As discussed in the next section, according to the XRD data, no carbonate (calcite, dolomite) was detected in the rock samples, and therefore, in the above-mentioned correction for Ca, only the correction for Ca in apatite was applied. This was further verified with an acid test on sample powders.

Increasing values of CIA and MIA from a crystalline rock are related to the formation of clay minerals such as illite or smectite first (CIA values of ~60 – 80) then kaolinite (CIA value of 100), and reflect removal of labile cations relative to stable Al in the clays [22].

For the studied basalt samples CIA and MIA varies between 37.2 – 39.1 and 34.1 – 37.0, respectively. The CIA and MIA values are within the range expected for fresh basalt [30] such that there remains a significant component of Al-bound Ca and Mg in magmatic minerals (plagioclase, pyroxene) available for release during alteration. Any amygdale-hosted minerals seem not to have significantly modified the chemistry.

For the studied sandstone samples, the CIA values are between 63.5 and 65.9, indicating that the combination of source weathering and hydrodynamic sorting have increased the abundance of clay minerals relative to feldspars in typical igneous source rocks. The MIA is not considered since direct comparison to a source rock (or rocks) cannot be made with current data and could include a more felsic rock. Regardless, from the perspective of this work, the low Ca and Mg content of these samples indicate limited reaction potential for CO_2 mineralization.

The Index of Compositional Variability (ICV) is a measure of compositional maturity of a rock and is calculated as follow [32]:

$$\mathrm{ICV} = (\mathrm{Fe_2O_3} + \mathrm{K_2O} + \mathrm{Na_2O} + \mathrm{CaO} + \mathrm{MgO} + \mathrm{MnO} + \mathrm{TiO_2})/\mathrm{Al_2O_3} \quad (6)$$

ICV values higher than 1.0 indicate immature rocks composed of non-clay silicate minerals, whereas mature rocks containing abundant clay minerals show low ratios of the major cations to Al_2O_3 and have low ICV values (less than 1.0). Generally, low ICV values and high CIA and MIA values suggest highly weathered rocks [22]. In this study, ICV values of the basalt samples varies between 2.21 and 2.44. This further confirms the low chemical alteration of these samples. The ICV values for the sandstone samples are however, lower than 1.0, except for the sample SW-13 where the ICV is 1.12, indicating moderate alteration of these rocks.

The powder X-ray diffractograms of the selected basalt and sandstone samples, are shown in Fig. 4 and Fig. 5, respectively.

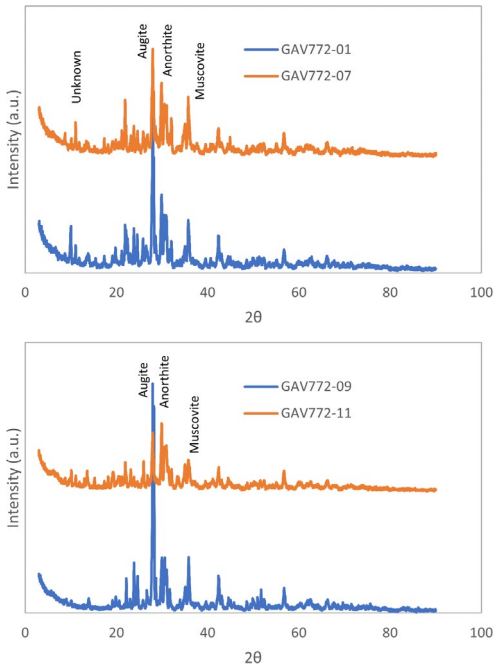

Fig. 4. Powder X-ray diffractograms of selected basalt samples.

The major phases in the selected basalt samples are pyroxenes, with augite (typical best-match for XRD peaks similar to: $FeCa_4Si_8Mg_{2.96}O_{24}$) or diopside (typical best-match for XRD peaks similar to: $MgCaSi_2O_6$) as representative, and plagioclase feldspar, with anorthite ($CaAl_2Si_2O_8$) or some slightly more Na-enriched solid-solution member identified as representative. Other minor phases appear to be a K-bearing phyllosilicate represented by muscovite ($Kal_2(AlSi_3O_{10})(OH)_2$), and a range of alteration-related phyllosilicates (specific identification in progress; low 2θ angle peaks) associated with either partial groundmass and phenocryst replacement or amygdule in-fills.

XRD results indicate quartz to be the most abundant mineral in the studied sandstone samples with other minor phases to be albite and kaolinite. This is consistent with weathering and erosion of sources that include more felsic rocks than just basalt, followed by further sedimentary processes such as fluvial hydrodynamic sorting.

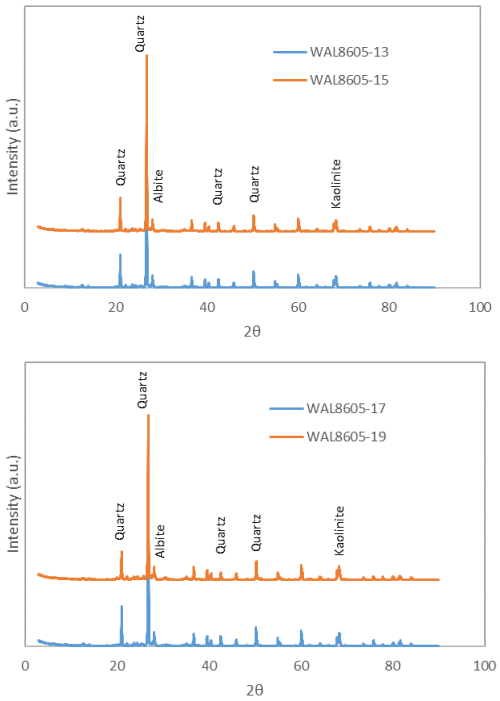

Fig. 5. Powder X-ray diffractograms of selected sandstone samples.

5 Conclusions

The petrophysical assessment tests revealed that the porosity of the basalt samples is below 10.2%, with the lowest amount as 2.4%. The majority of the sandstone samples have porosity values above 10.0%. Moreover, the basalt samples show low permeabilities, i.e., below 0.17 mD. Higher permeability values were obtained for the sandstone samples, with the highest value of 3.36 mD. The mineralogical and geochemical studies showed that the basalt samples are mostly composed of augite and anorthite with significant reaction potential to release Ca and Mg, critical for CO_2 mineralization, upon further alteration. As per the sandstone samples, quartz was found to be the major phase with albite and kaolinite as minor phases in the rock samples with very limited reaction potential to release elements favourable for CO_2 mineralization. While the basalt formations exhibit promising mineralization potential, the current permeability values suggest that direct CO_2 injection into these tight formations would be challenging. This necessitates either the identification of higher permeability zones within the basalt or the implementation of engineering interventions to enhance permeability. For the sandstone formations, although permeability is relatively higher, their limited mineralization potential suggests they may not be as effective for long-term CO_2 trapping through mineralization.

These findings underscore the need for further comprehensive testing and analysis to better understand the porosity-permeability relationship and to identify zones with enhanced injectivity. Future phases of this project will focus on expanding the dataset and comparing it with global benchmarks to provide more concrete recommendations for CO_2 storage site selection and optimization.

Acknowledgments

We would like to thank the Geological Survey of Canada (GSC) for their technical assistance and financial support. We thank the Core Research Equipment & Instrument Training Network (CREAIT) at Memorial University for the use of their XRD and XRF facilities within The Earth Resources Research and Analysis (TERRA) Facility. The authors would like to thank the Hibernia Management and Development Company (HMDC), the Natural Sciences and Engineering Research Council of Canada (NSERC), Dept of Energy, Industry and Technology, Government of Newfoundland and Labrador, and Mitacs for financial supporting the Hibernia Research Lab and its staff.

References

1. M.D. Aminu, S.A. Nabavi, C.A. Rochelle, V. Manovic, Appl. Energy, 208, 1389-1419 (2017).
2. P. Kelemen, S.M. Benson, H. Pilorge, P. Psarras, J. Wilcox, Frontiers in Climate, 1-20 (2019).
3. V.I. Fagorite, C.F. Chijioke, A.I. Opara, S.O. Onyekuru, E.E. Oguzie, Euro-Mediterr. J. Environ. Integr., 445-461 (2022.)
4. S.J. Friedmann, Elements, **3,** 179-184 (2007).
5. M. Andrew, B. Bijeljic, M.J. Blunt, Geophys. Res. Lett., **40,** 3915-3918 (2013).
6. Q. Hu, Q. Wang, T. Zhang, C. Zhao, K.H. Iltaf, S. Liu, Y. Fukatsu, Energy Reports, **9,** 3661-3682 (2023).
7. J. Pronost, G. Beaudoin, J. Tremblay, F. Larachi, J. Duchesne, R. Hebert, M. Constantin, Environ. Sci. Technol., **45,** 9413-9420 (2011).
8. F. Bahr, D. Keighley, Can. J. Earth Sci., **58,** 209-224 (2021).
9. J.W.F. Waldron, M.C. Rygel, M.R. Gibling, J.H. Calder, Geol. Soc. Am. Bull, **125**, 945-960 (2013).
10. R.J. Ryan, R.C. Bohner, J.H. Calder, B. Can. Petrol. Geol., **39,** 289-314 (1991).
11. A.G. Plint, G.H. Browne, J. Sediment. Res., **B64,** 341-364 (1994).
12. M.C. Rygel, C. Lally, M.R. Gibling, A. Ielpi, J.H. Calder, A.R. Bashforth, Atl. Geol., **51,** 1-43 (2015).
13. Gulf Resources, Hastings No.1 Well History Report, 45p. (1975).
14. J. Wade, D. Brown, A. Traverse, R. Fensome, Atl. Geol., **32,** 189-231 (1996).
15. S. Cirilli, A. Marzoli, L. Tanner, H. Bertrand, N. Buratti, F. Jourdan, G. Bellieni, D. Kontak, P. Renne, Earth Planet. Sci. Lett., **286,** 514-525 (2009).
16. D.J. Kontak, Lithos, **101,** 74-101 (2008).
17. J.D. Keppie, Digital version of Nova Scotia Dept. of Natural Resources Map ME-2000-1 (2006).
18. N. Schleifer, E. Kesse, G. Lawrence, SCA2018-047 (2018).
19. I. Pinerez, T. Puntervold, S. Strand, P. Hopkins, P. Aslanidis, H.S. Yang, M.S. Kinn, J. Pet. Sci. Eng., **195,** 107654 (2020).
20. L. Klinkenberg, American Petroleum Institute: Washington, DC, USA., (1941).
21. C. McPhee, J. Reed, I. Zubizarreta, Elsevier (Amsterdam, Netherlands). 64, 181-267 (2015).
22. F. Perri, Palaeogeography, Palaeoclimatology, Palaeoecology, **556,** 109873 (2020).
23. B. Hazra, A.K. Varma, A.K. Bandopadhyay, S. Chakravarty, J. Buragohain, S.K. Samad, A.K. Prasad, J. Nat. Gas Sci. Eng., **32,** 239-255 (2016)
24. P. Oliva, J. Viers, B. Dupré, Chem. Geol., **202,** 225-256 (2003).
25. G. Raab, F. Scarciglia, K. Norton, D. Dahms, D. Brandová, R. de Castro Portes, M. Christl, M.E. Ketterer, A. Ruppli, M. Egli, Land Degrad. Dev., **29,** 3736-3752 (2018).
26. C.M. Fedo, H.W. Nesbitt, G.M. Young, Geology, **23,** 921-924 (1995).
27. S.M. McLennan, D.K. Hemming, G.N. Hanson, Geol. Soc. Am. Spec. Pap., **284,** 21-40 (1993).
28. H.W. Nesbitt, G.M. Young, Nature, **299,** 715-717 (1982).
29. L. Harnois, Sediment. Geol., **55,** 319-322 (1988)
30. M.G. Babechuk, M. Widdowson, B.S. Kamber, Chem. Geol., 363, 56-75 (2014).
31. M.G. Babechuk, C.M. Fedo, Can. J. Earth Sci., 60 (2023).
32. R. Cox, D.R. Lowe, R.L. Cullers, Geochim. Cosmochim. Acta, **59,** 2919–2940 (1995).